Virk, Usman; Haneda, Katsuyuki

Modeling Human Blockage at 5G Millimeter-Wave Frequencies

Published in:
IEEE Transactions on Antennas and Propagation

DOI:
10.1109/TAP.2019.2948499

Published: 01/03/2020

Document Version
Peer-reviewed accepted author manuscript, also known as Final accepted manuscript or Post-print

Please cite the original version:
Virk, U., & Haneda, K. (2020). Modeling Human Blockage at 5G Millimeter-Wave Frequencies. *IEEE Transactions on Antennas and Propagation*, *68*(3), 2256-2266. Article 8883197.
https://doi.org/10.1109/TAP.2019.2948499

Modeling Human Blockage at 5G Millimeter-Wave Frequencies

Usman Tahir Virk and Katsuyuki Haneda, *Member, IEEE*

***Abstract*—Millimeter-wave (mm-wave) spectrum unravels the humongous and accelerating demand for wireless data rates and, therefore, it will be a fundamental ingredient of the fifth-generation (5G) wireless technology. In case of mm-wave access links, humans are the most noticeable blockers of electromagnetic waves from access points to mobile stations and hence cause temporal variation in the radio channel. This paper presents human blockage measurements in the anechoic chamber at 15, 28 and 60 GHz frequencies employing 15 human subjects of different sizes and weights. An effective three-dimensional human blockage model as a double-truncated and absorbing multiple knife-edge (DTMKE) scheme is also proposed. By calculating diffraction from the DTMKE, the frequency, body orientation and antenna height dependency of the blockage are most accurately reproduced compared to the existing models, such as absorbing double knife-edge model and third generation partnership project (3GPP) human blockage model. The results demonstrate that the losses are proportional to the cross-section of the human body with respect to the radio link. Furthermore, the blockage loss decreases as the height of the transmitting antenna increases.**

***Index Terms*—Millimeter-wave (mm-wave), fifth-generation (5G), three-dimensional (3D), human blockage.**

I. Introduction

WIRELESS data traffic has been increasing at an enormous rate every year, and this tendency is expected to grow over the next decade with the high data rate video streaming applications and the Internet-of-Things (IoT) [1]. To meet this challenging demand, there is rapid development of the fifth generation (5G) cellular technology that will employ the millimeter-wave (mm-wave) frequency spectrum rendering several Gigabit-per-second (Gbps) data rates to user devices [2], [3]. Although there is a phenomenal bandwidth available at the mm-wave spectrum, yet it poses unique challenges for wireless communication systems [4]. This necessitates the development of suitable channel models at mm-wave frequencies where the propagation characteristics are not only influenced by large objects such as buildings, but also susceptible to much smaller obstacles such as cars, lampposts, and humans. With the vision of deploying mm-wave wireless systems mainly in urban open squares, streets and indoors, the third generation partnership project (3GPP) consider humans as one of the main obstacle affecting the mm-wave propagation and has thus included a blockage model into TR-38.901 of Release 14 [5]. Moving human bodies blocking mm-wave access links cause temporal variations in the radio channel [6].

Most human blockage models available in the literature [7]–[22] are physically articulate and evaluate the human blockage loss by considering body shape, dimension and material. These models provide reasonable accuracy at the cost of increased complexity in terms of geometrical description of the human body and computations. However, these models are not thoroughly validated for frequency, body size, orientation and antenna height dependency of the human blockage through measurements. A quantitative comparison of various existent human blockage models led us to investigate a more robust yet simple model for human blockage at mm-wave frequencies. Our robust and simple model is the main scientific merit.

The key contributions of this paper are threefold:

1) We present a detailed literature survey reviewing existing human blockage models and their quantitative comparison;
2) We report human blockage loss through anechoic chamber measurements at 15, 28, and 60 GHz employing 15 human subjects of different sizes and weights at each frequency band;
3) We propose a novel and simple yet an efficient three-dimensional (3D) human blockage model, called double-truncated and absorbing multiple knife-edge (DTMKE) model, that reproduces measured human body losses of the radio wave for various orientations of the body and heights of antennas that illuminate the body.

The remainder of the paper is organized in the following four sections: Section II provides a comprehensive literature review of available human blockage models and proposes a new efficient 3D human blockage model for mm-wave frequencies. Section III presents mm-wave human blockage measurements performed in the anechoic chamber at 15, 28, and 60 GHz with 15 human subjects of different sizes. Section IV compares the existing blockage models quantitatively for different body orientations and heights, and validates the proposed model with human blockage measurements to demonstrate its applicability. Finally, the paper is summarized and concluded in Section V.

II. Human Blockage Models

The available human blockage models typically define a blocking object through its shape and material. The blockage loss is determined by simple mathematical formulae, most

Manuscript received October 11, 2018; revised April 28, 2019 and August 14, 2019, accepted September, 08, 2019. Date of publication Month, XX, 2019, date of current version October 10, 2019. This work was supported by the Academy of Finland through the WiFiUS project—Device-to-Device Communications for Millimeter-Wave Frequencies under Grant 284709. *(corresponding author: Usman Tahir Virk.)*

U.T. Virk and K. Haneda are with the Department of Electronics and Nanoengineering, School of Electrical Engineering, Aalto University, FI-00076 Espoo, Finland (e-mail: usman.virk@aalto.fi; katsuyuki.haneda@aalto.fi).

of which are motivated by the diffraction of plane waves around blocking objects. The models are physically valid while their parameters such as shape, dimension, and material are statistically defined and determined to reproduce realistic losses. The major task of modeling human blockage is, therefore, to choose reasonable properties of the blocking objects. This section covers a review of available human blockage models that consider different shapes and material properties of the blocking objects for estimating the losses. The detailed mathematical description of these models is given in the Appendix. A similar survey comparing some popular human blockage models is available in [9], but covers only the distance-dependent human shadowing for frequencies up to 30 GHz. Hence, we complement this study by providing further insights into the body orientation and antenna height dependency of human blockage, which are the essential features when applying the model for cellular mobile access links.

A. Absorbing Screen Models

1) Double knife-edge diffraction model: The human body is popularly modeled as an absorbing screen where its shape is a vertically-infinitesimal strip and is known as double knife-edge diffraction (DKED) model [10]. It is possible to obtain reasonable estimates of the RX field across the body using DKED model where the diffracted fields from the two vertical sides of the screen are considered and is mathematically illustrated in Section A of the Appendix. Thanks to its simplicity, the DKED model of a human body is also used in estimating link attenuation when multiple human bodies block a propagation path [11], [12]. When absorbing screen is considered, the diffraction is independent of the polarization states of the incident field. For evaluating the human blockage attenuation more accurately, [13] modifies the DKED to account for the TX and RX antenna radiation patterns.

2) Multiple knife-edge diffraction model: In contrast to the DKED models where the human body is treated as a single infinitesimally-long absorbing strip along the z-axis, more complex human body blockage models not only accounts for the human torso but also shoulders and head [14]–[16] and are generally referred as multiple knife-edge diffraction (MKED) models. These are also absorbing screen models and considers diffraction from each edge of the absorbing screen to estimate the total blockage loss. Furthermore, the orientation of the human body leads to a variation in the human blockage loss; [14] characterizes the human blockage by assuming two vertical absorbing strips with the single-side truncation at the top of the strip resembling human head. The two strips intersect orthogonally and represent the width and thickness of a human body. Depending on the orientation of the two intersecting strips, only one of the two strips with the larger cross-section seen from the transmit (TX)–receive (RX) link is used for calculating the diffracted paths. A diffracted path from the top edge of the strip is considered in addition to the diffracted paths from the sides, leading to what is conveniently referred here as the single-truncated multiple knife-edge (STMKE) diffraction model, which is mathematically and visually illustrated in Section B of the Appendix.

The MKED models provide better agreement with measurements when the orientation of a human body is arbitrary and when mobile and base station antennas heights are different. They are important features in cellular mobile links, and are realized with increased complexity of the model.

B. Conducting Screen and Wedge Models

The paper [15] calculates the diffraction coefficients from each edge of a finitely conducting screen by assuming that each edge is a wedge with a zero wedge angle. In comparison with the MKED model, this model does not consider the screen as absorbing but rather as conducting or insulating. The uniform theory of diffraction (UTD) is employed for deriving the RX field [23] and is mathematically described in Section C of the Appendix. The diffraction coefficient from a finitely conducting wedge is also applicable to other types of shadowing objects than human bodies, e.g., building corners [24].

C. Cylinder Models

Human blockage models based on cylinders have also been popularly considered in the literature [7], [8], [18]–[20]. When a cylinder is circular in its cross-section and is a perfect electric conductor (PEC), closed-form polarimetric diffracted fields from the cylinder can be derived based on the geometrical theory of diffraction (GTD) [25], and is given in Section D of the Appendix. [18] also analyzed the effect of clothing on blockage loss and infers that clothing may influence the blockage loss under certain conditions and is sensitive to the thickness of clothing layer. Since cylinder gives the blockage loss independent of the orientation of a human body, a further improvement is considered by modeling the human body as an elliptical cylinder, which is mathematically explained in Section E of the Appendix. The solutions are for normal incidence of a plane wave to a cylinder, making it possible to analyze the scattering problem in two-dimensional (2D) space. When the scattering problem extends to 3D as oblique incidence of a plane wave to consider, e.g., scenarios with different heights of TX and RX antennas, closed form solutions of the scattering field do not exist. It is necessary to rely on a numerical electromagnetic field solver [17] and more extensive numerical integration [21] in this case.

D. Other Heuristic Models

The human blockage models discussed so far estimate the blockage loss by determining the diffracted fields across the blocking objects. Analytical formulae are available for calculating the diffracted fields, either based on the GTD or UTD solutions for simple objects such as absorbing screens, conducting edges and PEC cylinders. These formulae involve Fresnel integral (see (4) in Section A of the Appendix), which can be calculated using built-in functions available in many computational tools. However, they may still be considered too complex to implement in extensive radio network simulations. Alternatively, heuristic models are devised to simplify the GTD and UTD solutions with further approximations of the involved formulae, or observations and modeling of measurements.

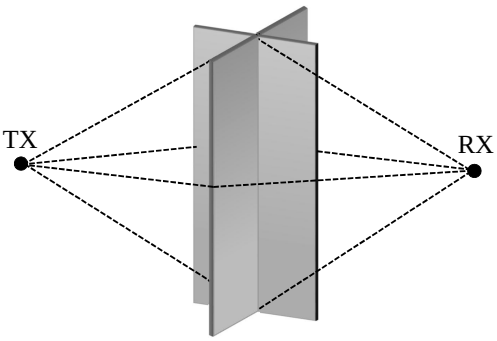

Fig. 1. Double-truncated multiple knife-edge (DTMKE) diffraction model.

1) Measurement-based models: Measurement-based models at mm-wave frequencies include, for example [26], that characterizes signal level attenuation due to human shadowing observed at short-range 60 GHz radio links using a Gaussian distribution. The work in [20] proposes a piecewise linear approximation of time-varying shadowing at 60 GHz due to human blockage. The approximation consists of a decreasing slope, shadowing dip and increasing slope of the received field strength as time goes during a human blockage event. The work in [27] models the transit rapid fading due to human blockage in pedestrian crowds via Markov process based on measurements in a dense urban environment at 73.5 GHz. The present paper excludes measurement-based models for further analysis as it is difficult to integrate them into link geometry.

2) 3GPP/mmMagic Model: A simplified GTD based blockage model is proposed in the European Union H2020-5GPPP project mmMagic [22], which is the improvement of the blockage model adopted by 3GPP TR−38.901 of Release 14 [5]. We classify this as a heuristic model since the formulae to predict the losses include approximations that do not follow physical intuition of the wave propagation. The detailed description of the model is given in Section F of the Appendix.

E. Proposed Double-Truncated Multiple Knife-Edge Model

We propose the double-truncated multiple knife-edge (DTMKE) human blockage model that considers the human body as a 3D screen, as illustrated in Fig. 1. DTMKE is based on the knife-edge diffraction from an absorbing screen. It is the improved STMKE model which is physically more intuitive as it considers an additional diffracting path between the legs of a human body, i.e., the bottom of the screen. In this model, the blockage loss is evaluated as the contribution of four diffracting paths from the screen i.e., the top, two sides and bottom. The field at the RX is thus given as

$$E_{\mathrm{DTMKE}} = \sum_{i=1}^{N} E_i \exp\left(-j2\pi f \frac{\Delta d_i}{c}\right), \qquad (1)$$

where E_i refers to the diffracting field corresponding to the $i-$th edge of the screen with $1 \leq i \leq 4$; Δd is the propagation distance of the diffracting path in excess to the line-of-sight (LOS) path; c is the speed of light and f is the center radio frequency. The field E in (1) is calculated from the knife-edge diffraction through the set of mathematical expressions (3)-(6) of the Appendix-A. The blockage loss is governed by the Fresnel-Kirchhoff parameter ν in (5), which physically represents the clearance height between the obstacle and LOS path multiplied by the frequency-dependent scalar. The clearance height is a function of the heights of screen, TX and RX. Evidently, as the TX height increases the blockage loss decreases and vice versa. Furthermore, it is necessary to consider the first Fresnel zone of the blocked path in relation to the cross-section of the blocking object to understand the extent of blockage loss. Majority of the electromagnetic wave energy is conveyed through the first Fresnel zone, and its cross-section becomes smaller as the frequency becomes higher. In the screen model of the human body, the screen in different azimuth orientations has varying effective widths with respect to the LOS path. Therefore, the blockage loss varies over azimuth orientations of the screen.

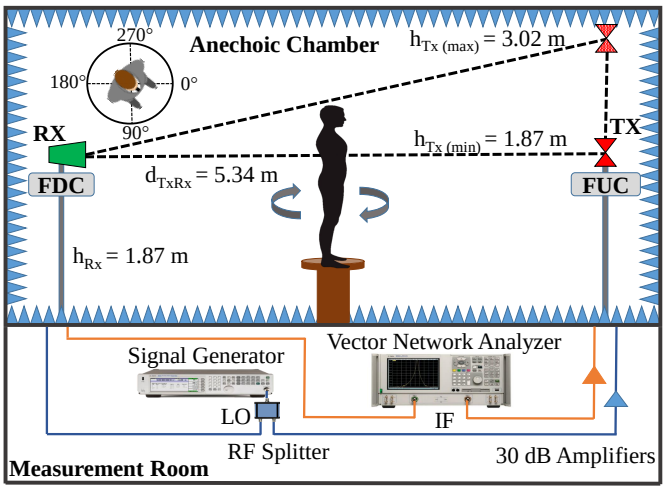

Fig. 2. Experimental setup and layout (FUC: Frequency up-converter, FDC: Frequency down-converter, LO: Local oscillator, IF: Intermediate frequency)

III. Millimeter Wave Human Blockage Measurements

A. Experimental Setup

A vector network analyzer (VNA) based measurement setup is employed for evaluating human blockage loss in a large anechoic chamber at three radio frequency (RF) bands, i.e. 15, 28 and 60 GHz. The setup is depicted in Fig. 2 where VNA is the central data acquisition component that measures the amplitude and phase of the received signal the complex channel transfer function $H(f_i)$ between TX and RX sides. The blockage measurements at 28 and 60 GHz are performed by mixing the VNA signals with the local oscillator (LO) signals using frequency up-converter (FUC) and down-converters (FDC). The experimental setup provide a varying dynamic range at each RF i.e., 70 dB to 85 dB from the highest to the lowest frequency band, respectively. Omni-directional bicone and sectoral horn antennas are used at the TX and RX sides, respectively. The TX and RX antennas used at the three measured frequency bands have similar gains and half-power beam widths (HPBW). The measurement parameters

TABLE I
ANECHOIC CHAMBER BLOCKAGE MEASUREMENTS PARAMETERS

Parameters	Frequency band		
	$f = 15$ GHz	$f = 28$ GHz	$f = 60$ GHz
IF signal (GHz)	n/a	$1-4$	$2.2-5.2$
LO signal (GHz)	n/a	13.5	14.7
RF signal (GHz)	$14-16$	$27-30$	$61-64$
Sweep points	3001		
TX antenna (Gain)	Bicone (2 dBi)		
HPBW (TX)	60°(elevation), omni-directional (azimuth)		
RX antenna (Gain)	H-plane sectoral horn (19 dBi)		
HPBW (RX)	40°(elevation), 10°(azimuth)		
EIRP (dBm)	17		
TX-RX height (m)	1.87		
TX-RX distance (m)	5.34		
Ref. meas.	Free-space without human subject		

IF: Intermediate frequency
HPBW: Half-power beam width
EIRP: Effective isotropic radiated power

along with the specifications of the TX and RX antennas are summarized in Table I.

In order to estimate the blockage loss, the measured channel with a human subject $H_{\rm S}(f_i)$ is calibrated by a free-space reference measurement without the human subject $H_{\rm C}(f_i)$, but with all the other components in the setup intact. The calibrated channel response $H_{\rm B}(f_i) = H_{\rm S}(f_i)/H_{\rm C}(f_i)$ is then converted to channel impulse response (CIR) $h(\tau)$ via inverse fast Fourier transform. Finally, the delay-gating is applied to isolate the signal component subject to human blockage from the unwanted reflections due to antenna mismatch and those originating from the environment. The human blockage loss $L_{\rm HB}$ is obtained as

$$L_{\rm HB} = \left\{ \max_{\tau_0 - w_{\rm g} \le \tau \le \tau_0 + w_{\rm g}} \left\| \frac{1}{N} \sum_{n=1}^{N} h_n(\tau) \right\| \right\}^{-2}, \qquad (2)$$

where $1 \le n \le N$ are indices of the CIR snapshots in a single body blockage measurement; $N = 80$ in this study and are averaged for reducing the noise level and small-scale fading effects. At 60 GHz where the wavelength is merely 5 mm, the measurements become more susceptible to small-scale fading effect and even a small movement of human subject may cause significant fluctuation of the received signal; $w_{\rm g}$ refers to the width of the delay-gating window and its value is chosen as 1.4 ns comparable to the average width of the measured human bodies; and τ_0 is the delay corresponding to the TX-RX separation or the LOS distance around which the peak is searched over the range of $2w_{\rm g}$. The peak search constraint in (2) is required to accurately isolate the main blockage path because: 1) the peak corresponding to it does not always appear at $h(\tau_0)$ and maybe slightly shifted due to measurement uncertainty, and 2) a strong diffracted path from the human body may appear in proximity of the LOS path. For the given RF bandwidths, a fine delay and spatial resolution of 0.5 ns and 15 cm are available at 15 GHz, while 0.33 ns and 10 cm are available at 28 and 60 GHz, respectively. .

TABLE II
SUMMARY OF THE BODY PARAMETERS OF HUMAN SUBJECTS.

S.No	Human Subjects	Height ($h_{\rm b}$) [m]	Weight [kg]	Average Body Width ($w_{\rm b}$) [m]	BMI[1]
1	A	2.05	68	0.45	16.18
2	B	1.78	67	0.45	21.15
3	C	1.68	61	0.44	21.61
4	D	1.78	69	0.46	21.78
5	E	1.68	62	0.45	21.97
6	F	1.92	84	0.51	22.79
7	G	1.73	71	0.44	23.72
8	H	1.77	75	0.47	23.80
9	I	1.87	83	0.56	23.88
10	J	1.84	82	0.50	24.22
11	K	1.48	53	0.41	24.20
12	L	1.66	69	0.47	25.04
13	M	1.74	77	0.48	25.43
14	N	1.88	90	0.50	25.46
15	O	1.78	82	0.50	25.90
16	P	1.94	90	0.49	23.91
17	Q	1.74	87	0.51	28.74
18	R	1.72	90	0.53	30.42
19	S	1.83	87	0.48	25.98
20	T	1.68	72	0.47	25.51
21	U	1.77	78	0.47	24.90

[1] $\text{BMI} = \dfrac{\text{weight (kg)}}{\text{height} \times \text{height (m}^2\text{)}}$

B. Measurement Scenarios

We evaluated the effect of human body orientation and height of TX antenna on human blockage, as illustrated in Fig. 2. The TX and RX antennas were separated by 5.34 m with a base height of 1.87 m above the floor of the anechoic chamber. The human subjects were located at the mid-point of the TX and RX antennas separation, which is the far-field region for the antennas at each frequency band i.e., $2D^2/\lambda$ where D is the maximum dimension of the antenna and λ is the wavelength. Furthermore, the human subjects were elevated from the ground with the aid of a 0.72 m high stool so that the LOS path is always blocked by the torso irrespective of the height of the human subjects. The human subjects are first rotated at different azimuth angles with respect to the LOS path in steps of 45°. The 0° or 180° represents the human body facing the TX or RX antenna, respectively, as shown in Fig. 2. TX and RX antennas were kept at the base height in the first measurements. In the second measurements, the human subject is kept at 0° position facing the TX antenna while the TX is elevated from the base height of 1.87 m to 3.07 m in steps of 0.15 m, as illustrated in Fig. 2.

Since the main propagation mechanisms of electromagnetic (EM) waves around the human body are diffraction at mm-waves, it is expected that the size and tissue contents of human body are the contributing factors in the blockage loss. Therefore, we considered 15 human subjects of different size and weight resulting in different body mass indexes (BMI) for evaluating human blockage loss at each frequency band. The parameters of human subjects are given in Table I.

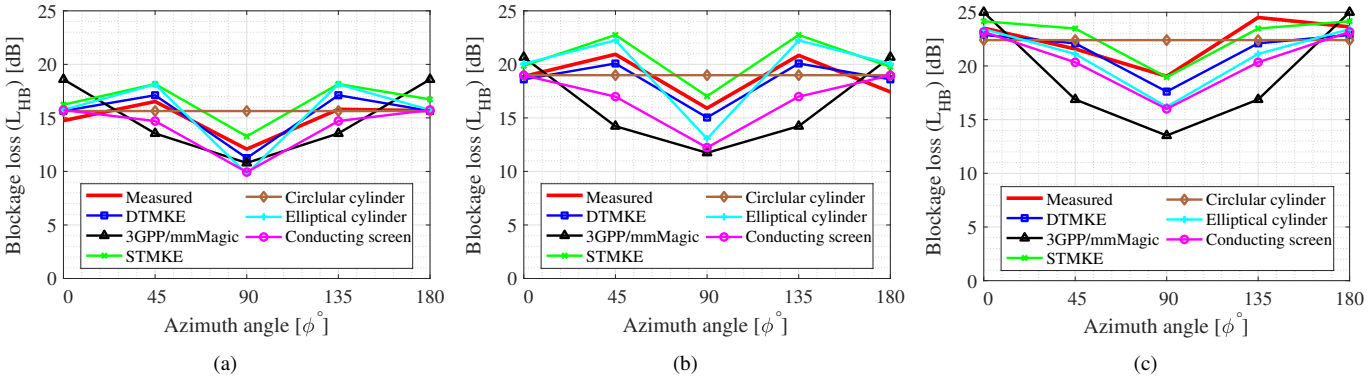

Fig. 3. Comparison of human blockage models with measurements for different body orientations at: (a) 15 GHz, (b) 28 GHz, and (c) 60 GHz.

IV. Results and Discussion

Section II presented various existing human blockage models and our proposed DTMKE model. Herein, we first briefly compare these models with measurements discussed in Section III to demonstrate the robustness of our model. The human blockage loss (L_{HB}) in Fig. 3, Fig. 4, and Fig. 6 is the median loss over all the 15 measured human subjects. We determine the relative height of the human subject with respect to the line-of-sight (LOS) path, also called as the LOS path-clearance, as $h = h_{\mathrm{b}} + h_{\mathrm{s}} - h_{\mathrm{RX}} - [(h_{\mathrm{TX}} - h_{\mathrm{RX}})/d] \cdot d_2$, where h_{b} is the absolute height of the human subject, h_{s} is the height of the stool, h_{TX} and h_{RX} are the antenna heights, d is the TX-RX antenna separation and d_2 is the distance between the RX antenna and the human subject; h is used in (4) of Section A of the Appendix.

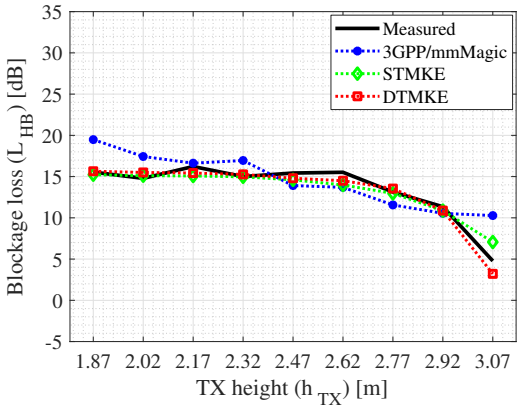

Fig. 4. Comparison of human blockage models with measurements in terms of median blockage loss (L_{HB}) over 15 human subjects at 15 GHz for different TX heights.

A. Comparison of models

Fig. 3 shows the median blockage loss over 15 human subjects estimated from different models covered in Section II and examined in contrast to the measurements. The comparison is made for various azimuth orientations of a human body at three different radio frequencies, i.e., 15, 28 and 60 GHz. The blockage loss is evaluated using physical parameters affecting the losses including TX-body-RX distance, TX and RX antenna heights, and the height and width of the human body. An average body thickness of 0.2 m is considered in the elliptic cylinder and STMKE models, and otherwise only the width is adopted to define the dimension of absorbing screens and circular cylinder. The azimuth orientation angle is defined such that the cross-section of a human body is largest at 0° and 180° because the human faces either the TX or RX, while 90° orientation corresponds to the human body parallel to the TX-RX link, as consistent with the coordinate system of the measurements. The curves labeled with "Conducting screen" are derived according to Section C of the Appendix for a PEC screen of the specified dimension. All the curves are for vertically polarized fields. Since measurements were conducted in anechoic chamber, it is safely assumed that significant reflections from the surrounding environment do not exist for these models. It is noteworthy in Fig. 3 that "Cylinder" models are 2D while the rest are 3D models. The blockage loss curves in Fig. 3 exemplifies that losses are proportional to the cross-section of the human body with respect to the link. The 2D models may underestimate blockage loss for some azimuth orientations of the body. For instance, in Fig. 3(a), the circular cylinder model being a coarse approximation of the human body and symmetric in all azimuth orientations, exhibits smaller loss at 45° compared to some of the 3D counterparts. The STMKE model, in general, offers more losses than the DTMKE model as it has a larger cross-section of the blocking object compared to the DTMKE. It is evident from Fig. 3 that DTMKE outperforms all other models at the three mm-wave frequency bands. To further illustrate the performance of the proposed DTMKE model, Fig. 4 shows an exemplary contrast of the 3D models including 3GPP/mmMagic, STKED, and DTMKE with measurements at 15 GHz for the varying TX height. We observe in Fig. 4 that the blockage loss decreases with the increase in TX height. Note that the DTMKE model at 28 and 60 GHz is also the best among the tested models though we do not show the results here due to space constraints. These results substantiate that our proposed model DTMKE accurately reproduces the frequency, body orientation and antenna height dependency of L_{HB} and outperforms the existing models.

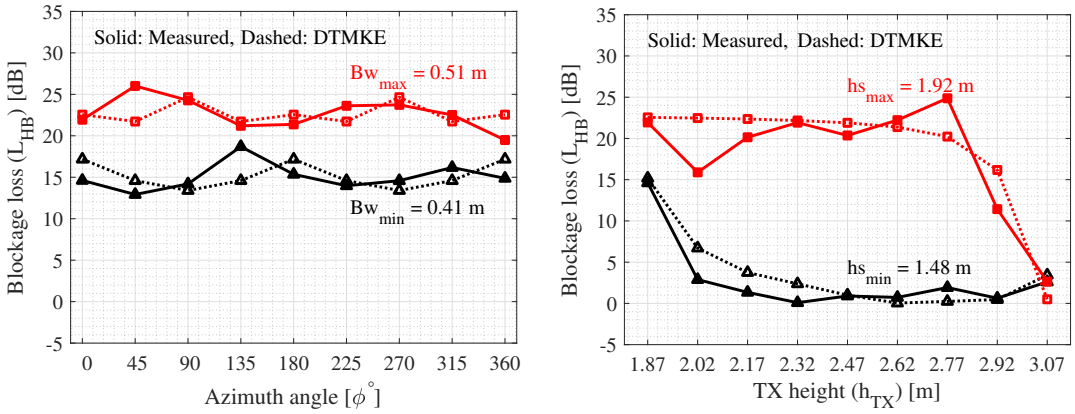

(a) (b)

Fig. 5. Measured and DTMKE-predicted human blockage loss (L_{HB}) comparison between human subject 'F' and 'K' with maximum and minimum body widths and heights, respectively, at 60 GHz frequency band for different: (a) body orientations and (b) TX heights.

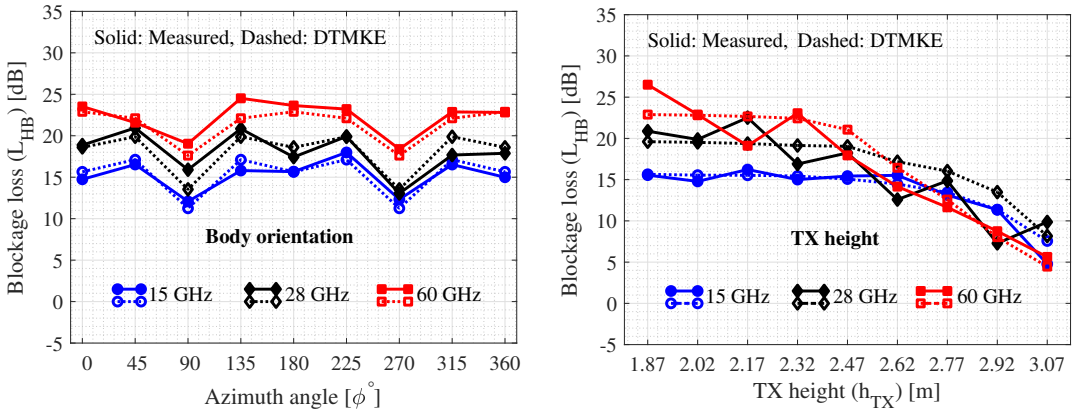

(a) (b)

Fig. 6. Measured and DTMKE-predicted median human blockage loss (L_{HB}) over 15 human subjects at 15, 28, 60 GHz frequency bands for different: (a) body orientations and (b) TX heights.

B. Validation of the proposed DTMKE model

For exemplifying the measured and DTMKE-predicted L_{HB} for a single human, we consider human subjects 'F' and 'K' that are consistently available in the three measured frequency bands and have maximum and minimum body widths (w_{b}) and heights (h_{b}), respectively, as given in Table I. Fig. 5(a) correlates L_{HB} between measurements and DTMKE for the widest 'F' and thinnest 'K' human subjects at 60 GHz for different body orientations. With the given geometry of the experimental setup, the width of the first Fresnel zone of the LOS link is 32.7 cm, 23.9 cm and 16.3 cm at 15, 28 and 60 GHz, respectively. The w_{b} corresponding to 'K' is 41 cm, which is greater than the size of first Fresnel zone at 15 GHz. This implies that all the human subjects used in this study completely blocked the first Fresnel zone at the given frequency bands. It is observed that the increasing w_{b} leads to greater L_{HB}, and hence, it is one of the key parameters in defining the human blockage. Fig. 5(b) illustrates the measured and estimated L_{HB} using DTMKE at different TX heights for the tallest 'F' and shortest 'K' human subjects facing the TX antenna perpendicular to the LOS path, i.e, 0°. It can be seen that 'F' causes more blockage loss compared to 'K' at almost all the TX antenna heights as LOS exists without blockage. This suggests that the h_{b} is also key parameter that governs the effect of human blockage when TX height is varied.

Fig. 6 analyzes the median L_{HB} over all the measured human subjects for the body orientation and TX height scenarios at the given frequency bands. In Fig. 6(a), we see that L_{HB} increases with the increase in frequency and is on average $7-10$ dB more at 60 GHz than at 15 GHz. The oblique orientation of the body to the TX-RX link tends to result in slightly greater L_{HB} compared to the cases where the human body is either parallel (90°) or perpendicular to the LOS path (0°). The standard deviations of losses for the body in different azimuth orientations are 1.94, 2.51, and 2.12 at 15, 28, and 60 GHz, respectively. Fig. 6(b) shows that L_{HB} decreases with the increase in TX height, by 10 dB at 15 GHz and 20 dB at 60 GHz between the transmitter height difference of 1.24 m. As long as the LOS path is obstructed, we see a clear difference of the L_{HB} at the three frequency bands. However, the blockage loss is smallest at 60 GHz when the TX antenna is at the highest position because the first Fresnel

zone of the link is obviously cleared. The confidential range of antenna heights for which the proposed model performs the best is the range used in the measurements, i.e., TX height from 1.87 m to 3.1 m and RX height of 1.87 m at 15, 28 and 60 GHz of the carrier frequency. We also found out that human body mass index (BMI) and $L_{\rm HB}$ do not show meaningful correlation. Our proposed DTMKE model is meant for humans with casual indoor clothing since it agrees meticulously with the measurements that were performed with humans wearing casual indoor clothing.

To quantify the measurement uncertainty, link blocking measurements with a body pointing to various angles in azimuth were carried out at each frequency band employing the human subject 'F' and repeated over a time difference of several hours. The mean standard deviations $\overline{\sigma}_{\rm m}$ of the blockage loss for the body in different azimuth orientations are 1.94 dB, 2.31 dB and 2.75 dB for 15, 28, and 60 GHz, respectively. Furthermore, the mean expanded uncertainties, $\overline{u}_{\rm e}$[1] [28], of the blockage loss at different angles over which the body was rotated are ± 0.79, ± 1.91, ± 1.97 dB for 15, 28 and 60 GHz, respectively. The expanded uncertainty ($u_{\rm e}$) shows the level of confidence of the estimates. Its mean values $\overline{u}_{\rm e}$ obtained here indicate that the measurement procedure for repeatability is under control. The observed differences of $L_{\rm HB}$ in Fig. 3-6 across body orientations, antenna heights and frequency are mostly greater than the mean expanded uncertainty and hence statistically significant.

V. Summary and Conclusions

Humans are the potential blockers of radio waves between mm-wave access points and mobile stations, thereby leading to temporal variation in the radio channel. This paper presented a comprehensive literature survey of the existing human blockage models and their quantitative comparison at 15, 28 and 60 GHz. The human blockage loss is characterized through anechoic chamber measurements with 15 human subjects of different sizes and weights. Finally, a novel 3D human blockage model based on absorbing and double-truncated multiple knife-edge diffraction is proposed. The proposed model predicts the measured human blockage losses more accurately than the existing models, such as absorbing single-truncated multiple knife-edge and 3GPP/mmMagic models. It was observed that the width, height and thickness of the human body are the key parameters influencing the human blockage and must be considered in blockage models. The blockage loss increases with the increase in frequency regardless of the human body orientations and is on average $7-10$ dB more at 60 GHz than at 15 GHz. For different body orientations, the blockage loss is proportional to the cross-section of the human body with respect to the link with standard deviations of 1.94, 2.51 and 2.12 at 15, 28, and 60 GHz, respectively. Furthermore, the human blockage loss decreases as the height of the transmitting antenna increases, by 10 dB at 15 GHz and 20 dB at 60 GHz between the transmitter height difference of 1.24 m. The more noticeable decrease at 60 GHz is due the clearance of the first Fresnel zone of the link as the transmit antenna is higher.

[1] $\overline{u}_{\rm e} = \sum_{n=1}^{N_{\rm a}} \pm k\left(\sigma/\sqrt{N_{\rm s}}\right)$ where σ is the standard deviation, $N_{\rm s} = 7$ is the number of repeatability samples, $N_{\rm a} = 9$ is the number of angles for which the body was rotated, and $k = 2$ is the coverage factor for 95% confidence.

Appendix

This appendix summarizes the mathematical description of the existing human blockage model for comparison among them and with measurements as shown in Fig. 3-6.

A. Absorbing Double Knife-Edge Diffraction

Consider a half-plane absorbing screen with TX and RX point sources, as illustrated in Fig. 8(a). The RX electric field is given by

$$E = \frac{1+{\rm j}}{2}\left\{\left(\frac{1}{2}-C(\nu)\right)-{\rm j}\left(\frac{1}{2}-S(\nu)\right)\right\}E_0, \quad (3)$$

where E_0 is the RX field when there is no absorbing knife edge; $C(\nu)$ and $S(\nu)$ are cosine and sine Fresnel integrals given by (7)

$$C(\nu)+{\rm j}S(\nu) = \int_0^{\nu}\exp\left({\rm j}\frac{\pi}{2}t^2\right){\rm d}t, \quad (4)$$

$$\nu = -h\sqrt{\frac{2}{\lambda}\left(\frac{1}{d_1}+\frac{1}{d_2}\right)}. \quad (5)$$

The formulae apply regardless of the polarization of the incident waves. The Fresnel integral (4) can be solved numerically using built-in functions of widely available computational software. (4) is subject to the conditions $d_1, d_2 \gg h$ and $d_1, d_2 \gg \lambda$. The relative field strength at RX across the absorbing screen can be calculated by considering the DKED problem Fig. 7(a) as two sub-problems that consist of half-plane absorbing screens with their diffracting edges corresponding to the sides of a human body. The diffracted field from each sub-problem is solved by (3), where the reference line-of-sight (LOS) field is given by

$$E_0 = \frac{\lambda}{4\pi(d_1+d_2)}\exp\left(-{\rm j}2\pi f\frac{d_1+d_2}{c}\right), \quad (6)$$

where c is velocity of light. The total field at the RX is expressed by the sum of the fields solved from the two sub-problems in [10] as

$$E_{\rm DKED} = E_{\rm A}\exp\left(-{\rm j}2\pi f\frac{\Delta d_{\rm A}}{c}\right)+E_{\rm B}\exp\left(-{\rm j}2\pi f\frac{\Delta d_{\rm B}}{c}\right), \quad (7)$$

where $E_{\rm A}$ and $E_{\rm B}$ are a diffracted field observed at RX, and $\Delta d_{\rm A} = d_{\rm TA}+d_{\rm AR}-d_1-d_2$, $\Delta d_{\rm B} = d_{\rm TB}+d_{\rm BR}-d_1-d_2$ are extra propagation distances of the two diffracted paths compared to the LOS, respectively.

B. Absorbing Multiple Knife-Edge Diffraction

When considering diffraction from multiple edges of an absorbing screen, any additional diffraction component is calculated using (3) and added to (7). For instance, as in the case of STMKE, the RX field is given by

$$E_{\rm STMKE} = E_{\rm DKED}+E_{\rm h}\exp\left(-2\pi f\frac{\Delta d_{\rm h}}{c}\right), \quad (8)$$

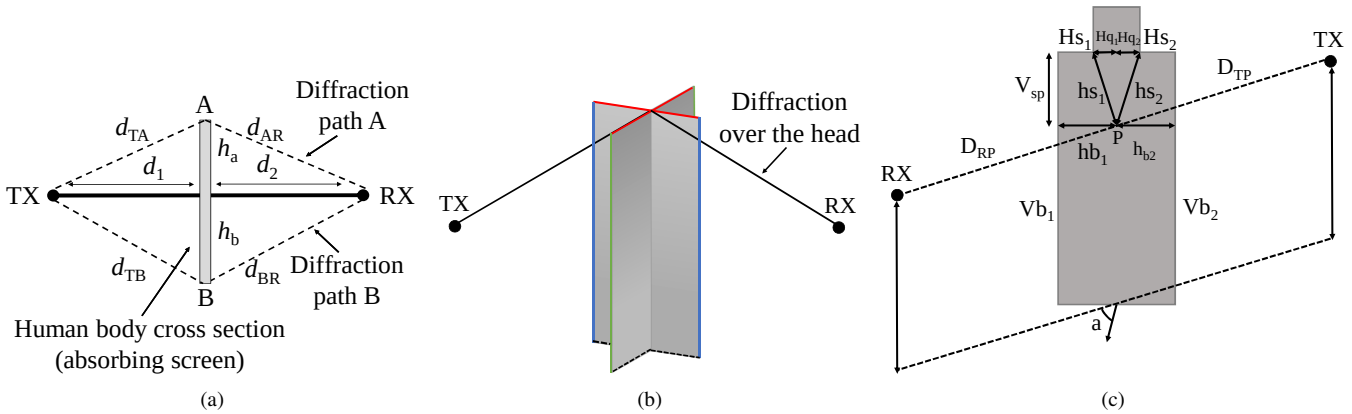

Fig. 7. Popular absorbing screen diffraction models of a human body: (a) Double knife-edge model [10], (b) Single-truncated multiple knife-edge model [14] and (c) Multiple knife-edge model with head and shoulders [16].

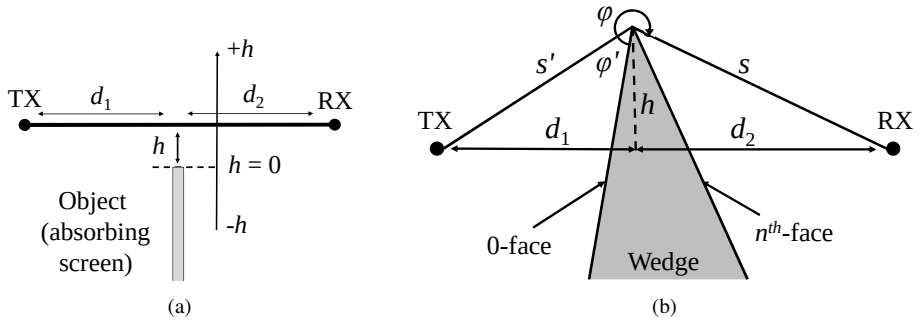

Fig. 8. (a) A half-plane absorbing screen and (b) a wedge between two points of TX and RX.

where $\Delta d_{\rm h} = d_{\rm THR} - d_1 - d_2$, $d_{\rm THR}$ is a three-dimensional distance between the TX source and RX observation point through the top edge of the half-plane vertical absorbing strip. While applying (3) to calculate the diffraction from each edge, the height h, distances d_1 and d_2 in (3) can be set by $h = h' \cos\alpha$, $d_1 = D_{\rm TP} \pm h' \sin\alpha$ and $d_2 = D_{\rm RP} \pm h' \sin\alpha$ for $h' = h_{\rm b1}, h_{\rm b2}, h_{\rm s1}$, $h_{\rm s2}$ for $-\pi/2 \le \alpha \le \pi/2$ as defined in Fig. 7(c). When the orientation of the human body is perpendicular to the TX-RX line, i.e., $\alpha \sim \pm\pi/2$, the thickness of the human body $w_{\rm b}$ is used instead of h. It is again noted that the diffraction coefficients do not depend on wave polarization because the human body is modeled as absorbing screens.

C. Conducting Screen and Wedge models

Given the wedge geometry depicted in Fig. 8(b), the diffracted field is given by

$$E_{\rm w} = E_0 \frac{e^{-{\rm j}ks'}}{s'} D^{\perp\|} \sqrt{\frac{s'}{s(s'+s)}} e^{-{\rm j}ks}, \tag{9}$$

where D is the diffraction coefficient of parallel and perpendicular polarizations, respectively. The function $F(\cdot)$ is the Fresnel integral as

$$F(x) = 2{\rm j}\sqrt{x} e^{{\rm j}x} \int_{\sqrt{x}}^{\infty} e^{-{\rm j}\tau^2} {\rm d}\tau, \tag{9}$$

and furthermore, in (8),

$$L = \frac{ss'}{s+s'}, \tag{10}$$

$$a^{\pm}(\beta) = 2\cos^2\left(\frac{2n\pi N^{\pm} - \beta}{2}\right), \tag{11}$$

$$\beta = \phi \pm \phi', \tag{12}$$

where n defines the exterior wedge angle to be $n\pi$ and $N^{\pm}$ are the integers that satisfy the following two equations,

$$2\pi n N^{+} - \beta = \pi, \quad 2\pi n N^{-} - \beta = -\pi. \tag{13}$$

Finally, $R_0^{\perp\|}$ and $R_n^{\perp\|}$ are the polarimetric Fresnel reflection coefficients of a plane wave at 0- and n-face, where incident and reflecting angles are given by ϕ' and $n\pi - \phi$, respectively. The possible singularity of the cotangent functions in (9) around the reflection and shadowing boundaries is mitigated through the approximation

$$\cot\left(\frac{\pi \pm \beta}{2n}\right) \cdot F(kLa^{\pm}\beta) \approx n\left[\sqrt{2\pi kL}\ {\rm sgn}\ \epsilon - 2kL\epsilon e^{{\rm j}\pi/4}\right] e^{{\rm j}\pi/4}, \tag{14}$$

with ϵ defined by

$$\beta = 2\pi n N^{\pm} \mp (\pi - \epsilon). \tag{15}$$

In this manner, it is possible to take into account realistic conductivity and permittivity of a human body. To improve

$$D^{\perp\parallel} = \frac{-e^{-\mathrm{j}\pi/4}}{2n\sqrt{2\pi k}} \times \left\{ \cot\left(\frac{\pi+(\phi-\phi')}{2n}\right)\cdot F(kLa^{+}(\phi-\phi')) + \cot\left(\frac{\pi-(\phi-\phi')}{2n}\right)\cdot F(kLa^{-}(\phi-\phi')) \right.$$
$$\left. + R_0^{\perp\parallel}\cot\left(\frac{\pi-(\phi+\phi')}{2n}\right)\cdot F(kLa^{-}(\phi+\phi')) + R_n^{\perp\parallel}\cot\left(\frac{\pi+(\phi+\phi')}{2n}\right)\cdot F(kLa^{+}(\phi+\phi'))\right\}. \quad (8)$$

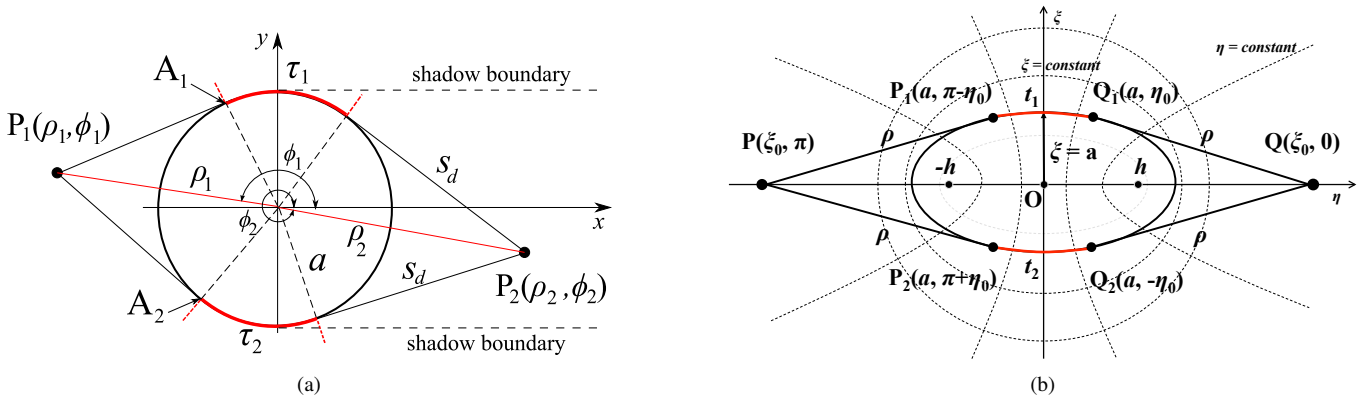

Fig. 9. (a) Circular [19] and (b) elliptical [29] cylinder models of link blockage.

the estimation of diffracted field from right-angle wedges, [30] proposes a different approximation of the diffraction coefficients using inverse problem theory. It is noteworthy that the wedge diffraction becomes a thin screen when $n = 2$, allowing us to calculate blockage loss due to finitely conducting screens using (9).

D. Circular Cylinder Model

Consider a circular cylinder with radius a as shown in Figure. 9(a). The field observed at point P_2 is given as a combination of the diffracted paths from the two sides of the cylinder namely,

$$E_z = \sum_{n=1}^{\infty} D_n^e E_i \left[\exp\left\{-(\mathrm{j}k+\Omega_n^{\mathrm{e}})\tau_1\right\} + \exp\left\{-(\mathrm{j}k+\Omega_n^{\mathrm{e}})\tau_2\right\}\right] \frac{\exp\left(-\mathrm{j}ks_{\mathrm{d}}\right)}{\sqrt{8\mathrm{j}\pi k s_{\mathrm{d}}}}, \quad (16)$$

where two propagation paths are of distances τ_1 and τ_2 and attenuated according to a constant Ω_n. For the electric field, this constant is given by

$$\Omega_n^{\mathrm{e}} = -\frac{q_n}{a} M e^{\mathrm{j}\pi/6}, \quad (17)$$

where $q_n = -\alpha_n$ denotes the n-th root (zero) of the Airy function $\mathrm{Ai}(\cdot)$ [31]. Finally, D_n and M are given by

$$D_n = 2M\mathrm{Ai}'(q_n)^{-2} e^{\mathrm{j}\pi/6}, \quad (18)$$
$$M = \left(\frac{ka}{2}\right), \quad (19)$$

where Ai' denotes as the derivative of the Airy function [31], and $k = 2\pi/\lambda$ is a wavenumber. It must be noted that the GTD solutions have singularity around the transition region between the lit and shadowed regions. Analytical UTD solutions for a conducting cylinder is limited, e.g., to a thin lossy material coating [32] and is valid only at sufficiently distant RX locations from the cylinder [33].

E. Elliptical Cylinder Model

Let us next consider a cylinder with an elliptic cross section. We assume that the center of the ellipse coincides with the z-axis of Cartesian coordinate system [29]. The distance between the two focal points of the ellipse is assumed to be $2h$. The elliptical coordinates on the horizontal plane, defined by ξ-η domain as depicted in Fig. 9(b), have a relationship with the Cartesian x-y coordinate as

$$x = h\cosh\xi\cos\eta, \quad y = h\sinh\xi\sin\eta. \quad (20)$$

In Fig. 9(b), the locations are expressed on the elliptic coordinate system as, e.g., $P(\xi,\eta)$. The ellipse representing the human cross section is given by $\xi = a$. The TX and RX antennas are located at $P(\xi_0,\pi)$ and $Q(\xi_0,0)$, respectively. Two diffracting rays symmetric to the horizontal axis exist from the TX antenna at P to the RX antenna at Q. The points of tangency where the two rays incident and leave the cylinder are $P_1(a,\pi-\eta_0)$, $Q_1(a,\eta_0)$, $P_2(a,\pi+\eta_0)$, and $Q_2(a,-\eta_0)$. The radial distance from the points of tangency to the Tx and Rx is $\overline{PP_1} = \overline{QQ_1} = \overline{PP_2} = \overline{QQ_2} = \rho$. The following derives the total field at the RX E_z for vertical polarization. First, the diffracted field at the RX due to the ray $\overline{PP_1Q_1Q}$ is

$$E_{1z} = A_0\rho^{-1}\exp\{\mathrm{j}k(\rho+t_1)\} \cdot \sum_{n=0}^{\infty} B_n(\eta_P)B_n(\eta_Q)\cdot\exp\left\{\mathrm{j}k^{1/3}\tau_n\alpha(t_1)\right\} \left[1-\exp\left\{\mathrm{j}kT+\mathrm{j}k^{1/3}\tau_n\alpha(T)\right\}\right]^{-1}, \quad (21)$$

where $\eta_P = \pi$ and $\eta_Q = 0$ are the η coordinates corresponding to the TX and RX locations P and Q, respectively; t_1 denotes

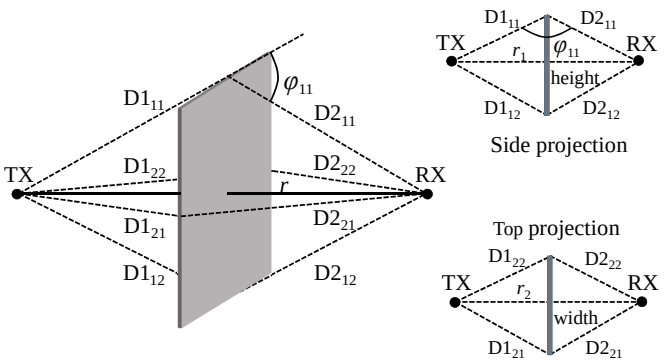

Fig. 10. Geometry of a link blockage model in [22]. The side and top views of the geometry are depicted at the top- and bottom-right of the figure and are referred as "projections 1 and 2", respectively, in the text.

the arc length from P_1 to Q_1 and T is the total arc length of the ellipse, A_0 is a constant given by

$$A_0 = \frac{e^{\mathrm{j}\pi/4}}{2\pi}\sqrt{\lambda}, \tag{22}$$

$B_n(\eta)$ represents the diffraction coefficient

$$B_n(\eta) = \pi^{3/4}2^{1/4}6^{-2/3}e^{j\pi/24}k^{-1/12}b^{1/6}(\eta)[\mathrm{Ai}'(q_n)]^{-1}, \tag{23}$$

where q_n is same as used in (18); $b(\eta)$ refers to the radius of the ellipse on the major axis as

$$b(\eta) = h(\cosh a \sinh a)^{-1}(\sinh^2 a - \sin^2 \eta + 1)^{3/2}. \tag{24}$$

Furthermore, in (21), $\alpha(x)$ is

$$\alpha(x) = \int_0^x b^{-2/3}(\eta)d\eta, \tag{25}$$

and τ_n is

$$\tau_n = e^{j\pi/3}6^{-1/3}q_n. \tag{26}$$

The diffracted field E_{2z} due to the ray $\overline{PP_2Q_2Q}$ can be evaluated in the same way as E_{1z}. Now the total diffracted field at the RX as a combination of the diffracted fields from the two sides of the elliptic cylinder is given as $E_z = E_{1z} + E_{2z}$.

F. 3GPP/mmMAGIC Model

The geometry of the blocking object is illustrated in Fig. 10 where the side and top views of the geometry shown on the right side of the figure are named as "projection 1 and 2" hereinafter, respectively. The blocking object is an infinitesimally thin rectangular screen floating in the air, and is claimed to be comprehensive enough to simulate different physical objects. The shadowing loss is determined for the screen as

$$E_{\mathrm{mmMAGIC}} = \left(1 - \prod_{i=1}^{2}\sum_{j=1}^{2} s_{ij}\left[\frac{1}{2} - \frac{ph_{ij}}{Ph}F_{ij}\right]\right)E_0, \tag{27}$$

where

$$F_{ij} = \left\{\frac{1}{2} - \frac{1}{\pi}\tan^{-1}\left(\frac{\nu_{ij}\pi}{2}\right)\right\}\cos\psi_{ij}, \tag{28}$$

$$\nu_{ij} = \sqrt{\frac{\pi}{\lambda}(D1_{ij}^{\mathrm{proj}} + D2_{ij}^{\mathrm{proj}} - r_i^{\mathrm{proj}})}, \tag{29}$$

$$ph_{ij} = \exp\left\{\frac{-\mathrm{j}2\pi}{\lambda}(D1_{ij} + D2_{ij})\right\}, \tag{30}$$

$$Ph = \exp\left(\frac{-\mathrm{j}2\pi}{\lambda}r\right). \tag{31}$$

Finally, s_{ij} is a sign parameter, which is 1 if the non-line-of-sight (NLOS) condition is in projection i while $s_{ij} = \mathrm{sgn}(D1_{ij} + D2_{ij} - D1_{ik} - D2_{ik})$ if the LOS condition is in projection i, where $k = \mod(j, 2) + 1$. It is noteworthy that the *multiplication* of fields from different sides of the absorbing screen in (27) is an approximation which is not physically intuitive for wave propagation, and hence, we regard this model as heuristic. The term $\cos\psi_{ij}$ in F_{ij} accounts for increase of shadowing loss in the shadowed zone behind the screen. For the large distances relative to the screen, this factor may be neglected. The formulation fulfills the Babinet principle, according to which different shapes of the blocking objects such as a truck [22] may be synthesized by combining multiple screens.

ACKNOWLEDGMENT

The authors would like to thank all the colleagues and students who volunteered as human subjects for the mm-wave blockage measurements. The authors also appreciate Reza Naderpour and Abbas Nezhad Manavi for their assistance in measurements.

REFERENCES

[1] ITU-R, "IMT traffic estimates for the years 2020 to 2030," International Telecommunication Union, Recommendation ITU-R M.2370-0, 2015.

[2] T. S. Rappaport *et al.*, "Millimeter wave mobile communications for 5G cellular: It will work!" *IEEE Access*, vol. 1, pp. 335–349, May 2013.

[3] T. S. Rappaport, Y. Xing, G. R. MacCartney, A. F. Molisch, E. Mellios, and J. Zhang, "Overview of millimeter wave communications for fifth-generation (5G) wireless networks-with a focus on propagation models," *IEEE Trans. Ant. Propag.*, vol. 65, no. 12, pp. 6213–6230, Dec 2017.

[4] T. S. Rappaport, G. R. MacCartney, S. Sun, H. Yan, and S. Deng, "Small-scale, local area, and transitional millimeter wave propagation for 5G communications," *IEEE Trans. Ant. Propag.*, vol. 65, no. 12, pp. 6474–6490, Dec 2017.

[5] 3GPP, "Study on channel model for frequencies from 0.5 to 100 GHz (release 14)," 3GPP, resreport TR 38.901 V14.1.1, July 2017.

[6] M. Gapeyenko, A. Samuylov, M. Gerasimenko, D. Moltchanov, S. Singh, M. R. Akdeniz, E. Aryafar, N. Himayat, S. Andreev, and Y. Koucheryavy, "On the temporal effects of mobile blockers in urban millimeter-wave cellular scenarios," *IEEE Trans. Veh. Tech.*, vol. 66, no. 11, pp. 10 124–10 138, Nov 2017.

[7] M. Ghaddar, L. Talbi, and T. A. Denidni, "Human body modelling for prediction of effect of people on indoor propagation channel," *Electr. Lett.*, vol. 40, no. 25, pp. 1592–1594, Dec 2004.

[8] M. Ghaddar, L. Talbi, T. A. Denidni, and A. Sebak, "A conducting cylinder for modeling human body presence in indoor propagation channel," *IEEE Trans. Ant. Propag.*, vol. 55, no. 11, pp. 3099–3103, Nov 2007.

[9] W. Qi, J. Huang, J. Sun, Y. Tan, C. X. Wang, and X. Ge, "Measurements and modeling of human blockage effects for multiple millimeter wave bands," in *Proc. 13th International Wireless Commun. Mobile Comput. Conf. (IWCMC'17)*, Valencia, Spain, June 2017, pp. 1604–1609.

[10] J. Kunisch and J. Pamp, "Ultra-wideband double vertical knife-edge model for obstruction of a ray by a person," in *Proc. IEEE Int. Conf. Ultra-Wideband*, vol. 2, Hannover, Germany, Sep 2008, pp. 17–20.

[11] M. Jacob, S. Priebe, T. Kürner, M. Peter, M. Wisotzki, R. Felbecker, and W. Keusgen, "Extension and validation of the ieee 802.11ad 60 GHz human blockage model," in *Proc. 7th European Conf. Ant. Propag. (EuCAP'13)*, Gothenburg, Sweden, Apr 2013, pp. 2806–2810.

[12] J. S. Lu, D. Steinbach, P. Cabrol, and P. Pietraski, "Modeling human blockers in millimeter wave radio links," *ZTE Commun. Mag.*, vol. 10, no. 4, pp. 23–28, Dec 2012.

[13] G. R. MacCartney, S. Deng, S. Sun, and T. S. Rappaport, "Millimeter-wave human blockage at 73 GHz with a simple double knife-edge diffraction model and extension for directional antennas," in *Proc. IEEE 84th Veh. Tech. Conf. (VTC-Fall'16)*, Montreal, Canada, Sep 2016.

[14] M. Jacob, S. Priebe, A. Maltsev, A. Lomayev, V. Erceg, and T. Kürner, "A ray tracing based stochastic human blockage model for the IEEE 802.11ad 60 GHz channel model," in *Proc. 5th European Conf. Ant. Propag. (EUCAP'11)*, Rome, Italy, Apr 2011, pp. 3084–3088.

[15] N. Tran, T. Imai, and Y. Okumura, "Study on characteristics of human body shadowing in high frequency bands: Radio wave propagation technology for future radio access and mobile optical networks," in *Proc. 80th IEEE Veh. Tech. Conf. (VTC-Fall'14)*, Vancouver, Canada, Sep 2014.

[16] X. Chen, L. Tien, P. Tang, and J. Zhang, "Modelling of human body shadowing based on 28 GHz indoor measurement results," in *Proc. IEEE 84th Veh. Tech. Conf. (VTC-Fall'16)*, Montreal, Canada, Sep 2016.

[17] M. Yokota, T. Ikegamai, Y. Ohta, and T. Fujii, "Numerical examination of em wave shadowing by human body," in *Proc. 4th European Conf. Ant. Propag. (EuCAP'10)*, Barcelona, Spain, Apr 2010.

[18] M. Jacob, S. Priebe, T. Kürner, M. Peter, M. Wisotzki, R. Felbecker, and W. Keusgen, "Fundamental analyses of 60 GHz human blockage," in *Proc. 7th European Conf. Ant. Propag. (EuCAP'13)*, Gothenburg, Sweden, Apr 2013, pp. 117–121.

[19] C. Gustafson and F. Tufvesson, "Characterization of 60 GHz shadowing by human bodies and simple phantoms," in *Proc. 6th European Conf. Ant. Propag. (EUCAP'12)*, Prague, Czech Republic, Mar 2012, pp. 473–477.

[20] M. Peter, M. Wisotzki, M. Raceala-Motoc, W. Keusgen, and R. Felbecker, "Analyzing human body shadowing at 60 GHz: Systematic wideband MIMO measurements and modeling approaches," in *Proc. 6th European Conf. Ant. Propag. (EUCAP'12)*, Prague, Czech Republic, Mar 2012, pp. 468–472.

[21] A. G. Aguilar, P. H. Pathak, and M. Sierra-Pérez, "A canonical UTD solution for electromagnetic scattering by an electrically large impedance circular cylinder illuminated by an obliquely incident plane wave," *IEEE Trans. Ant. Propag.*, vol. 61, no. 1, pp. 5144–5154, Oct. 2013.

[22] M. Peter and (ed.), "Measurement results and final mmmagic channel models: Specular wall reflections and diffused scattering measurements," Millimetre-Wave Based Mobile Radio Access Network for Fifth Generation Integrated Communications (mmMAGIC), resreport H2020-ICT-671650-mmMAGIC/D2.2, May 2017. [Online]. Available: https://bscw.5g-mmmagic.eu/pub/bscw.cgi/d202656/mmMAGIC_D2-2.pdf

[23] R. Luebbers, "Finite conductivity uniform GTD versus knife edge diffraction in prediction of propagation path loss," *IEEE Trans. Ant. Propag.*, vol. 32, no. 1, pp. 760–766, Jan. 1984.

[24] M. Jacob, S. Priebe, R. Dickhoff, T. Kleine-Ostmann, T. Schrader, and T. Kurner, "Diffraction in mm and sub-mm wave indoor propagation channels," *IEEE Trans. Microw. Theory Techn.*, vol. 60, no. 3, pp. 833–844, March 2012.

[25] G. James, *Geometrical Theory of Diffraction for Electromagnetic Waves, Ch. 6*. Stevenage, U.K.: Peregrinus, 1976.

[26] P. Karadimas, B. Allen, and P. Smith, "Human body shadowing characterization for 60 GHz indoor short-range wireless links," *IEEE Ant. Wireless Propag. Lett.*, vol. 12, pp. 1650–1653, Dec 2013.

[27] G. R. MacCartney, T. S. Rappaport, and S. Rangan, "Rapid fading due to human blockage in pedestrian crowds at 5G millimeter-wave frequencies," in *IEEE Global Communications Conference (GLOBECOM)*, Singapore, Dec 2017.

[28] "Evaluation of measurement data - Guide to the expression of uncertainty measurements," Bureau International des Poids et Mesures (BIPM), ISO/IEC- JCGM 100:2008, Septemebr 2008.

[29] B. R. Levy, "Diffraction by an elliptic cylinder," *J. Mathematics and Mechanics*, vol. 9, no. 2, pp. 147–165, Nov. 1960, [Online]. Available: http://www.jstor.org/stable/24900530.

[30] H. Wang and T. S. Rappaport, "A parametric formulation of the UTD diffraction coefficient for real-time propagation prediction modeling," *IEEE Ant. Wireless Propag. Letters*, vol. 4, pp. 253–257, 2005.

[31] M. Abramowitz and I. A. Stegun, *Handbook of mathematical functions: with formulas, graphs, and mathematical tables*. Courier Corporation, 1964, vol. 55.

[32] H.-T. Kim and N. Wang, "UTD solution for electromagnetic scattering by a circular cylinder with thin lossy coatings," *IEEE Trans. Ant. Propag.*, vol. 37, no. 11, pp. 1463–1472, Nov. 1989.

[33] T. B. A. Senior and J. L. Volakis, *Approximate Boundary Conditions in Electromagnetics*. London, U.K.: The Institution of Electrical Engineers, 1995.

Usman Tahir Virk received the B.Sc. EE degree in electronics and telecommunications from University of Engineering and Technology, Lahore, Pakistan, in 2007. From 2007 to 2010, he was associated with the telecom industry in Pakistan as an O&M Engineer. He received the M.Sc. Tech. (Hons.) degree from Aalto University, Espoo, Finland in 2012, where he is pursuing his D.Sc. Tech degree in radio engineering. He is currently working as Senior R&D Engineer at Keysight Technologies, Finland. He is the recipient of Best Student Paper awards at the Loughborough Antennas and Propagation Conference (LAPC2015), Loughborough, United Kingdom and the 11th European Conference on Antennas and Propagation (EuCAP2017), Paris, France. He also received Nokia Foundation Scholarship 2017 in recognition of his doctoral research. He has been actively involved in research collaborations with other universities and industry for 5G radio channel modeling. His research interests include multi-band radio channel measurements, simulations and modeling focusing millimeter-wave (mm-Wave) frequencies for 5G systems and beyond, Radio Frequency (RF) and mm-Wave material characterization, massive MIMO, smart antennas, electromagnetic scattering problems, full-wave numerical techniques, wireless communications for medical applications, MIMO Over-the-Air (OTA) and radio channel emulation.

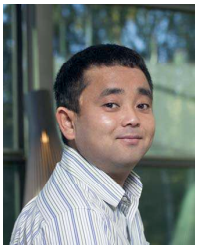

Katsuyuki Haneda (S03, M07) received the Doctor of Engineering from the Tokyo Institute of Technology, Tokyo, Japan, in 2007. Dr. Haneda is presently an associate professor in Aalto University School of Electrical Engineering. He is the recipient of the best paper award of the antennas and propagation track in the IEEE 77th Vehicular Technology Conference (VTC2013-Spring), Dresden, Germany, and of the best propagation paper award in the 7th European Conference on Antennas and Propagation (EuCAP2013), Gothenburg, Sweden. Dr. Haneda has been an associate editor of the IEEE Transactions on Antennas and Propagation between 2012 and 2016, and of an editor of the IEEE Transactions on Wireless Communications since 2013. He has also been an active member of a number of European COST Actions, e.g., CA15104 Inclusive Radio Communication Networks for 5G and beyond (IRACON), where he is a co-chair of a disciplinary working group on radio channels. His current research activity includes high-frequency radios such as millimeter-wave and beyond, wireless for medical, post-disaster scenarios and internet-of-things, and in-band full-duplex radio technologies.